Modeling Daily Temperatures Via a Phenology-Based Annual Temperature Cycle Model

Haiping Xia, Yunhao Chen, Adu Gong, Kangning Li, Long Liang, and Zhen Guo

***Abstract*—High spatiotemporal resolution land surface temperature (LST) plays an important role in various environment applications. However, the limitation of thermal infrared sensors and the effect of clouds and other atmospheric conditions result in discontinuous daily thermal observations of the Moderate Resolution Imaging Spectroradiometer (MODIS). Annual temperature cycle (ATC) models can help to supply daily continuous LSTs via limited observations, but these ATC models seldom consider the disturbance of weather conditions or the land cover change. On the other hand, spatial interpolation techniques also limit in implementation when available data in one day or several days are not able to obtain enough spatiotemporal information for LST reconstruction. The objective of this study is to propose a phenology-based ATC model (termed PATC), which takes the phenology change and local weather change into account, to reconstruct daily unscanned LSTs at an annual scale. Daily MODIS LSTs collected in 2015 were utilized to analyze the performance of PATC compared with other ATC models. Results show that PATC improved the accuracy by 1.6 and 0.5 K compared to the classic ATC model in the daytime and nighttime, respectively. Compared to the enhanced ATC model, PATC also shows better performance with higher accuracies, especially during the growing season of vegetation in the daytime. Future research may focus on an incorporation with Landsat observations and diurnal temperature cycle models to implement LST reconstruction at a diurnal scale.**

***Index Terms*—Annual temperature cycle (ATC), land surface temperature (LST) reconstruction, Moderate Resolution Imaging Spectroradiometer (MODIS), phenology.**

I. Introduction

LAND surface temperature (LST), which estimated from satellite thermal infrared (TIR) sensors, is a key parameter in monitoring evapotranspiration [1], [2], modeling surface energy balance [3], analyzing urban heat island (UHI) effect [4], [5], and detecting thermal anomaly [6]. However, those TIR images are low tolerant to clouds which almost bring half missing data to the LST time series [7]−[10], accordingly affects the applications of LSTs on environmental analysis.

To fill out these spatiotemporal gaps, a number of spatial interpolation and temporal interpolation techniques were put forward. The spatial interpolation methods tend to be data-driven and focus more on the spatial details on a specific date. According to the source of reference information, they can be generally grouped into two types: 1) spatial information based and 2) spatiotemporal information based. With the spatial information, the kriging geostatistical technique [11], inverse distance weighting (IDW) [12], and clustering inverse distance weighting (C-IDW) [13] could be applied for spatial interpolation. In addition, some auxiliary data such as normalized difference vegetation index (NDVI) and elevation were also utilized as predictors for regression to incorporate with the LST reconstruction process [14]. Fan *et al*. [15] even evaluated three regression tools and suggested that regression tree performed better than linear regression and artificial neural networks in flat and fragmented areas. However, spatial information from one day might not always be effective in some situations; hence, spatiotemporal information from adjacent dates was used to enable this interpolation. The spatiotemporal information based methods, such as the neighborhood similar pixel interpolator [16], geostatistical neighborhood similar pixel interpolator [17], and weighted linear regression algorithm [18], were proposed to make up for the insufficient spatial information. These methods were not initially designed for LSTs; so they seldom consider the characteristics of LSTs. Therefore, Shuai *et al*. [19] introduced the reflectance for similar pixels searching in the LST reconstruction process based on an assumption that the same land cover types have similar LST locally. Similarly, some spatiotemporal-based interpolation methods aiming at LSTs were also implementing calculations via regression between multitemporal LSTs within similar pixels [20], [21].

Temporal interpolation methods are different from spatial interpolation methods in aims and principles, but they can be used for gap filling as well. Specifically, spatial interpolation methods designed for LSTs could utilize the spatiotemporal information from auxiliary data (e.g., multitemporal LSTs or NDVI), but they act less robust when the gap is large [16], [22], [23]. On the contrary, temporal interpolation methods designed for LSTs [e.g., annual temperature cycle (ATC) models] can fully fill temporal gaps with several observations [23]. Some hybrid methods that combine temporal interpolation and spatial interpolation technique together use temporal interpolation technique for gap filling instead, when missing data accounts for

Manuscript received March 10, 2021; revised April 24, 2021; accepted May 27, 2021. Date of publication June 1, 2021; date of current version June 30, 2021. This work was supported in part by Beijing Natural Science Foundation under Grant 8192025, in part by the Projects of Beijing Advanced Innovation Center for Future Urban Design, Beijing University of Civil Engineering and Architecture under Grant UDC2019031321, and in part by the Beijing Laboratory of Water Resources Security, and in part by National Natural Science Foundation of China under Grant 41601468 *(Corresponding authors: Yunhao Chen and Adu Gong.)*

Haiping Xia, Yunhao Chen, Adu Gong, Kangning Li, and Long Liang are with the State Key Laboratory of Remote Sensing Science, Faculty of Geographical Science, Faculty of Geographical Science, Beijing Normal University, Beijing 100875, China (e-mail: xiahp93@mail.bnu.edu.cn; cyh@bnu.edu.cn; gad@bnu.edu.cn; lknkiki@mail.bnu.edu.cn; lianglong@mail.bnu.edu.cn).

Zhen Guo is with the National Satellite Meteorological Center, Beijing 100081, China (e-mail: guozheng@cma.gov.cn).

Digital Object Identifier 10.1109/JSTARS.2021.3085342

a large amount and the spatially interpolated result cannot meet with demand [24].

Temporal interpolation methods usually use sporadic observations to estimate consecutive data at different timescales [25]. Some of these temporal interpolation methods use singular spectrum analysis [26], temporal Fourier analysis [27], or a principal component analysis [28] for data reconstruction, of which many of them were not initially designed for LSTs. In addition, most of these temporal interpolation methods rely on the physical or statistical models to describe the temporal variations of temperatures [28]−[31]. Specifically, at a diurnal timescale, various diurnal temperature cycle (DTC) models that consist of several parameters are used for temperature modeling [32]−[38]. While at an annual timescale, ATC models [29], [31] play an important role in the temporal interpolation processes instead. Moreover, the annual predictions can also serve for diurnal temporal interpolations [35], thermal sharpening [39], [40], and analyzing of UHIs [4], [41] and public health [42].

The ATC models used to predict daily LSTs can be generally divided into two groups. The first group requires only the multitemporal temperature observations, which consists of one or two sine functions [43], [44] or even a series of harmonic functions [30]. Some methods incorporating an ATC model with a linear trend for multiyear LST modeling can also be classified into this group [43], [45]. These algorithms are designed based on the LST without any other auxiliary data, and they have common in the assumption that the temporal variation of LSTs is primarily driven by the solar radiation [29], [30], [44]. The second group uses not only multitemporal LSTs but also a series of auxiliary data such as the *in situ* surface air temperature (SAT), NDVI, and albedo [23], [46] to take the local synoptic conditions and land cover change into account. These kinds of methods are combinations of multiple harmonics and a linear function of LST-related factors, which can help the model adapt to different scenarios [23]. However, existing ATC models seldom consider the response of vegetation to phenology in mixed pixels. When the observed object consists of vegetation which has significant phenological changes in a year (e.g., turning green or turning brown), single or multiple harmonics, even those linear regression model may not be able to simulate the daily temperature variation well.

Therefore, the objective of this article is to propose a phenology-based ATC model (termed PATC) for time series LST reconstruction, which takes the response of vegetation to phenology into account. Here, we used daily day/night LSTs of the Moderate Resolution Imaging Spectroradiometer (MODIS) to implement this method. Study area and data are provided in Section II. The details of the method and implementation process are provided in Section III. Results and discussions are presented in Sections IV and V. Finally, Section VI concludes this article.

II. Study Area and Data

A. Study Area

Beijing, Tianjin, and Hebei provinces located in the North China Plain with a semihumid continental monsoon climate are selected as the study area. Specifically, this study area has a rainy and hot summer and a dry and cold winter, whose spring and autumn are extremely short. The study area [see Fig. 1(b)] is mainly covered by cropland and grassland, and the elevation ranges from −6 to 2764 m with a mean elevation of 506 m. Since the land cover consists of large amount of vegetation and the four seasons are distinct in this study area, the phenology changes significantly. These characteristics make this study area an ideal place to test the model performance at a regional scale.

B. Data

The satellite data used in this study include the MODIS daily LST product MOD11A1, 16-day NDVI product MOD13A2, and the MODIS yearly land cover product MCD12Q1 in 2015 (download from https://ladsweb.modaps.eosdis.nasa.gov/). Specifically, the MODIS LSTs in collection 6 were retrieved via the generalized split-window algorithm with a mean error within 1.0 K which were proved to be better than the previous C4.1 and C5 products [47]−[49]. The daytime and nighttime LSTs of the MOD11A1 were acquired at around 10:30 A.M. and 10:30 P.M., respectively. In addition, the Shuttle Radar Topography Mission digital elevation model (DEM) image with a resolution of 90 m was downloaded from http://www.gscloud.cn/. The resolutions of the MOD13A2, DEM, and MCD12Q1 were resampled to 1 km to match that of the LST product. Moreover, the NDVI product derived from the MOD13A2 is a 16-day composite; hence, we applied a thin plate spline interpolation to make it daily available.

Apart from those satellite data, daily maximum and minimum SATs from 27 meteorological stations [see Fig. 1(b)] downloaded from http://data.cma.cn/site/ were also used here. These SATs were resampled into 1-km resolution raster images via IDW method to match the LST products [46].

III. Method

In this section, we first introduce the classic ATC model and the enhanced ATC model (ATCE) and then we provide a detailed description of PATC. The model diagram and flowchart of PATC is provided in Fig. 2.

A. Classic ATC Model

The temporal interpolation of PATC is composed of various ATC models. Here, we utilize the classic ATC model which consists of three parameters [29] and we term it ATC in this study. The equation of ATC is as follows:

$$\varphi_{\mathrm{ATC}}\ (T_0, A, \theta, d) = T_0\ + A \cdot \sin\left(2\pi d/365 + \theta\right) \quad (1)$$

where φ_{ATC} is the predicted LST via the ATC model, d represents the day of the year, and T_0, A, and θ are the mean LST, amplitude, and phase shift of the annual LST cycle, respectively. These parameters are obtained via a Levenberg−Marquardt scheme [50] in the IDL platform.

Since the ATC model tends to smooth LSTs temporally [23], there are always residuals remaining between the observations and predictions. Hence, the observed LSTs can be expressed as

$$T\ (d) = \varphi_{\mathrm{ATC}}\ (T_0, A, \theta, d) + \Delta T\,(d) \quad (2)$$

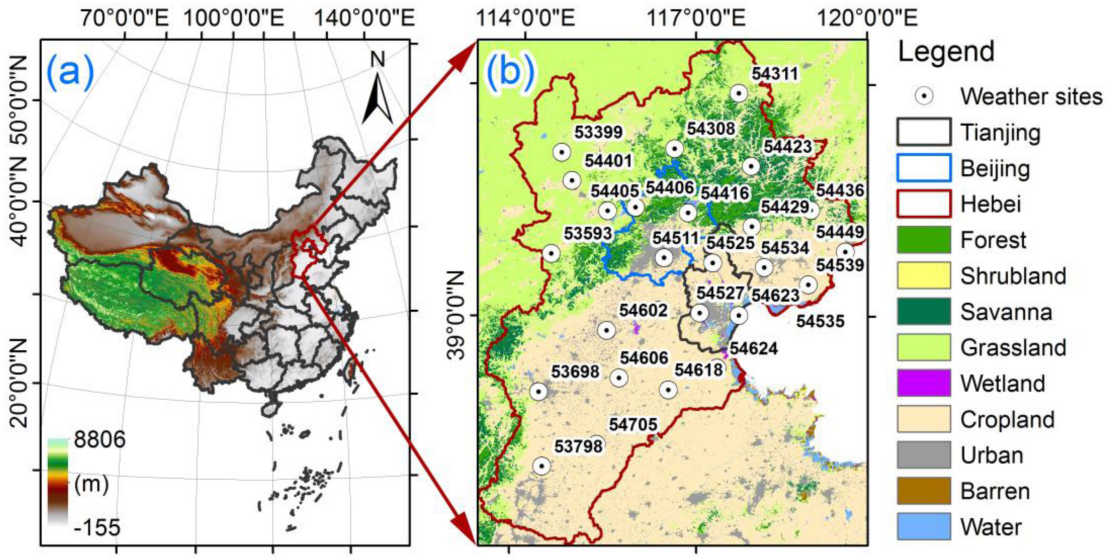

Fig. 1. Study area. (a) DEM of China. (b) Land cover map of Beijing, Tianjin, and Hebei provinces (obtained from MODIS yearly land cover product in 2015).

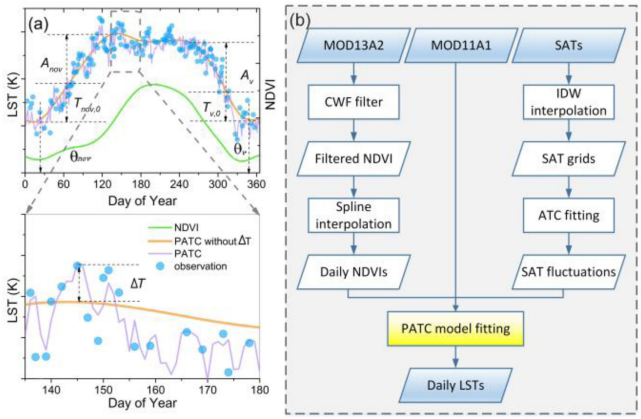

Fig. 2. Model diagram and flowchart of PATC. (a) Model diagram of PATC. (b) Flowchart of PATC.

where $T(d)$ is the observed LST on the dth day, and $\Delta T(d)$ is the residual between the observation and the prediction on the dth day.

B. Enhanced ATC Model

The ATCE model assumes that the annual surface temperature dynamics are mainly controlled by the solar radiation flux at the top of the atmosphere. In addition to solar radiation, the surface temperature is also controlled by the climatic background and local weather conditions, leading to short-term fluctuations of the surface temperature [46]. Therefore, the model can be expressed as follows:

$$T_{\mathrm{ATCE}}\ (d) = T_0\ + A \cdot \sin\left(\frac{2\pi d}{365} + \theta\right) + \Delta T_{\mathrm{air}}\,(d) \cdot \gamma\,(d) \tag{3}$$

where $T_{\mathrm{ATCE}}(d)$ is the predicted LST on the dth day, ΔT_{air} is the temperature fluctuations caused by weather conditions, and $\gamma(d)$ is the phenological factor, and can be expressed by following equation:

$$\gamma\ (d) = \lambda \cdot \left(\mathrm{NDVI}_{\max} - \mathrm{NDVI}_{\min}\right) / \left[\mathrm{NDVI}\,(d) - \mathrm{NDVI}_{\min} + 1\right] \tag{4}$$

where λ is the multiplier factor and $\mathrm{NDVI}_{\min}$ and $\mathrm{NDVI}_{\max}$ are the minimum and maximum NDVI values in a year, respectively; $\mathrm{NDVI}(d)$ is the NDVI value on the dth day. In addition, the air temperature fluctuations can be calculated by following equation:

$$\Delta T_{\mathrm{air}}\ (d) = T_{\mathrm{air}}\ (d) - T_{\mathrm{ATC,air}}\,(d) \tag{5}$$

where $T_{\mathrm{air}}(d)$ is the maximum/minimum air temperature on the dth day, and $T_{\mathrm{ATC,air}}(d)$ is the maximum/minimum air temperature simulated by ATC model, which can be calculated by (1). Specifically, the maximum air temperature is used for calculation in the daytime, while the minimum air temperature in the nighttime.

C. Phenology-Based ATC Model

Due to the heterogeneity of the land surface, when the thermal signal in an endmember is smaller than the pixel size, the pixel will respond to the thermal signal of multiple endmembers [35], and the mixing effect of the pixel will be enhanced with the reduction of resolution. The linear temperature mixing model (LTMM) assumes that the temperature of the mixed pixel is a weighted linear combination of different endmember components [51]. Therefore, considering the mixing effect of pixels, the PATC assumes that the surface temperature of a pixel is a linearly weighted combination of vegetated and nonvegetated fractions. In addition, considering the influence of local weather, the PATC also regresses surface temperature fluctuations caused

by weather conditions and air temperature fluctuations for temperature reconstruction (see in Fig. 2). Therefore, the formula of PATC, which takes both phenological changes and local weather effects into account, is as follows:

$$T_{\mathrm{PATC}}\ (d) = f_v\ (d) \cdot \left[T_{v,0} + A_v \cdot \sin\left(\frac{2\pi d}{365} + \theta_v\right)\right] + f_{\mathrm{nov}}\,(d) \cdot \left[T_{\mathrm{nov},0} + A_{\mathrm{nov}} \cdot \sin\left(\frac{2\pi d}{365} + \theta_{\mathrm{nov}}\right)\right] + \Delta T\,(d) \tag{6}$$

where $T_{\mathrm{PATC}}(d)$ is the predicted LST via PATC on the dth day, f_v is the fraction of vegetation in a mixed pixel, and f_{nov} is fraction of nonvegetation in a mixed pixel, and it can be calculated by $f_{\mathrm{nov}} = 1 - f_v$; $T_{v,0}$, A_v, and θ_v are the annual mean temperature, amplitude, and phase of the vegetation fraction, respectively, and $T_{\mathrm{nov},0}$, A_{nov}, and θ_{nov} are the annual mean temperature, amplitude, and phase of the nonvegetation fraction, respectively; ΔT is the fluctuations of LST, and it can be obtained through the statistical regression with temperature fluctuations. The equation is as follows:

$$\Delta T\ (d) = k \cdot \Delta T_{\mathrm{air}}\,(d) + b \tag{7}$$

where k and b are the slope and the intercept, and ΔT_{air} is the fluctuation of air temperature, and can be calculated by (5).

Meanwhile, the vegetation fraction can be calculated by the following equation:

$$f_v = \left(\frac{\mathrm{NDVI} - \mathrm{NDVI}_{\min}}{\mathrm{NDVI}_{\max} - \mathrm{NDVI}_{\min}}\right) \tag{8}$$

where $\mathrm{NDVI}_{\min}$ and $\mathrm{NDVI}_{\max}$ are the minimum and maximum NDVI values, respectively.

Since MODIS products only provide 16-day synthetic NDVI and are subject to weather conditions (such as cloud and atmospheric disturbances), NDVI products for different dates have different noise levels. Therefore, the changing-weight filter method [52] is adopted in this study to remove noise of the NDVI products. After removing noise, spline interpolation was used to obtain daily NDVI data. The flowchart can be seen in Fig. 2.

IV. Result

A. Spatial and Temporal Patterns of PATC

In this section, we present the spatial and temporal patterns of PATC and compare them with the classic ATC model. The evaluation indicators used in this study include root mean square error (RMSE) and difference of RMSE (Drmse). Compared with classic ATC, PATC performs better in both daytime and nighttime with a lower RMSE of 3.1 K for the daytime and 2.5 K for the nighttime, while those of classic ATC are 4.7 K for the daytime and 3.0 K for the nighttime. The higher RMSEs of both PATC and ATC in the daytime compared to those in nighttime might be due to the higher LST variations during daytime [46]. As shown in Fig. 3, the RMSEs of classic ATC are higher in the northern area of which the land cover type is mainly grassland and terrain is complex, and they are lower in the southern area of which the land cover type is mainly cropland and the terrain is flat. The spatial pattern of PATC's RMSEs is similar to that of classic ATC, of which the RMSEs are slightly lower in the southeast of the study area and higher in the northwest. However, the Drmse (referenced to classic ATC) of PATC is higher in the northern area, which indicates a higher improvement in areas covered by grassland and wherein the terrain is complex [see Fig. 3(c) and (f)]. In addition, the temperature difference of vegetation and bare soil components in mixed pixels is larger in the daytime than that in the nighttime, which decreases the accuracy of the temperature cycle model in the daytime. The Drmse in the nighttime is also lower than that in the daytime with a mean value of 0.5 K, which is due to the more homogeneous LST in the nighttime [see Fig. 3(c) and (f)].

To evaluate the improved accuracy of PATC evaluated via Drmse (referenced to classic ATC) response to land cover types, the classified Drmses are provided in Fig. 4. Results show that the improvements over grassland are higher than those over

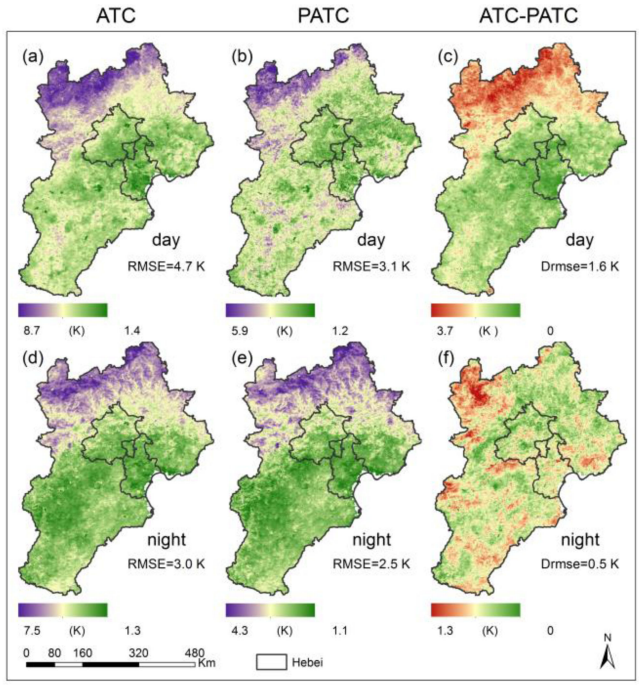

Fig. 3. RMSEs of classic ATC and PATC, and Drmse of PATC (referenced to classic ATC) in daytime and nighttime, respectively.

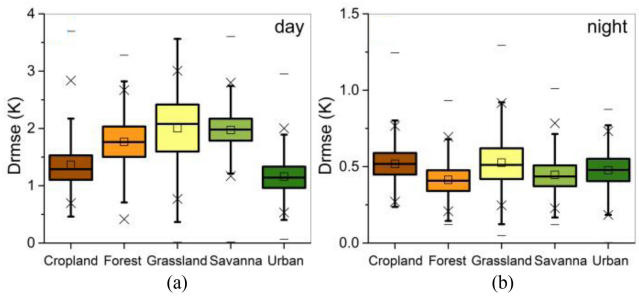

Fig. 4. Drmse of PATC (referenced to classic ATC) over different land cover types in daytime and nighttime, respectively.

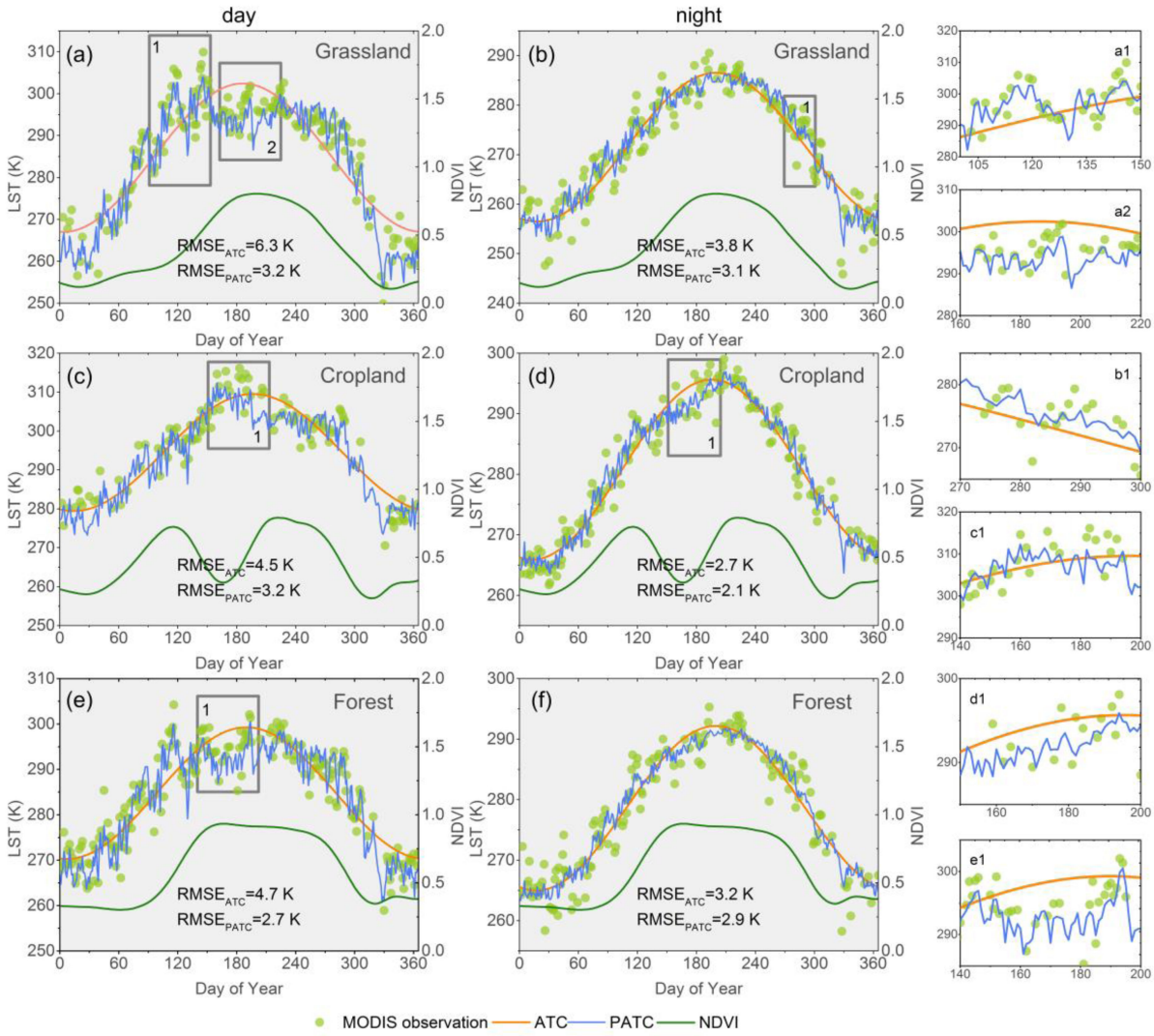

Fig. 5. Comparisons of model performances of PATC and classic ATC at daily scale in daytime and nighttime. (a1), (a2), (b1), (c1), (d1), and (e1) are the subfigures from the first and second columns. The $\mathrm{RMSE}_{\mathrm{ATC}}$ and $\mathrm{RMSE}_{\mathrm{PATC}}$ represent the RMSEs of classic ATC and PATC, respectively.

other land covers in both daytime and nighttime. In the daytime, the grassland presents the largest mean Drmse of 2.0 K, while the urban area presents the lowest with 1.2 K, and the mean Drmses of cropland, forest, and savanna are 1.4, 1.8, and 1.7 K, respectively. In the nighttime, the difference of Drmses of various land cover types is smaller, that almost of them are at around 0.5 K, wherein the Drmses of grassland are slightly higher. The lower Drmses in the nighttime are because the temperature difference between vegetation and nonvegetation fractions is larger in the daytime than that in the nighttime; accordingly, the superiority of the application of LTMM in the nighttime is not as obvious as that in the daytime.

Above results show the spatial pattern of the performance of PATC. To evaluate the performance of PATC temporally, three pixels located in three different land cover types are selected to show the results of PATC, the land covers of which are grassland, cropland, and forest, respectively. Here, we also supply NDVI variation corresponding to the LSTs to explain the fluctuation of LST observations. As shown in Fig. 5, the predicted LST via PATC can reliably catch the short-term variations of LSTs caused by the weather change and phenology change, while that via classic ATC tends to smooth these fluctuations. For example, as shown in Fig. 5(a2), the vegetation fraction in the mixed pixel increases when the grassland starts growing; hence, the temperature of the mixed pixel decreases by the transpiration of vegetation in the daytime [53]. Meanwhile, the ATC curve cannot totally catch the variations of observations and the RMSE of which is 6.3 K, while PATC curve fits these observations quite well and the RMSE of which is 3.2 K [Fig. (5a)]. As shown in Fig. 5(c), in the cropland, the vegetation fraction starts to decrease when the vegetation enters its first end of season (EOS); hence, the LST of the mixed pixel is improved due to the highly reflected sunlight in the daytime. Meanwhile, the temperature fluctuations are well simulated by PATC of which the RMSE is improved by 1.3 K compared with the classic ATC model. On the contrary, the vegetation fraction will not cool the surface [54] but increases the LST [55] in the nighttime. Specifically, the decreased vegetation fraction of the cropland decreases the LST

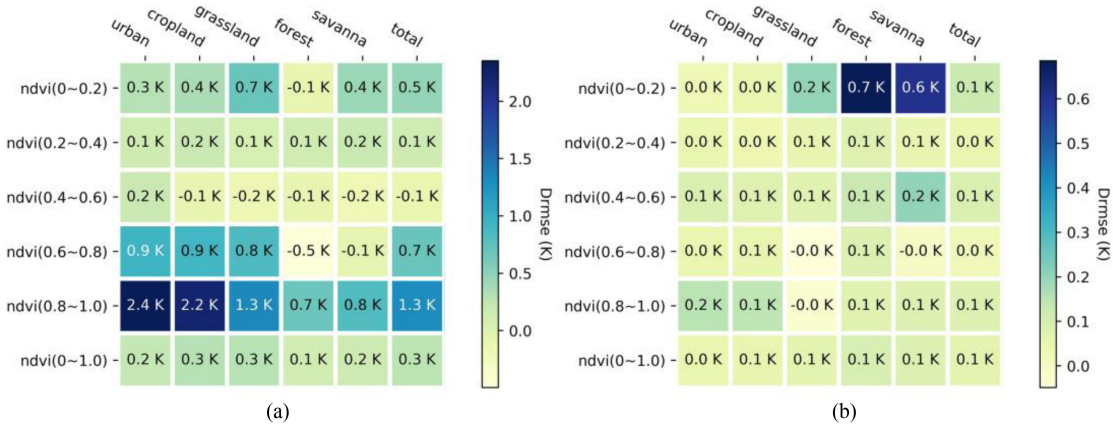

Fig. 6. Drmse (referenced to ATCE) of PATC over different land cover types in daytime and nighttime, respectively. (a) Drmse in daytime. (b) Drmse in nighttime.

in the nighttime during its first EOS. The temperature fluctuation is not as evident as that in the daytime, but it still can be caught by PATC [see Fig. 5(d1)]. As shown in Fig. 5(e), in the forest, the LST decreases due to the cooling effect of vegetation when the vegetation fraction reaches 1, the temperature fluctuation of which is well predicted by PATC model, while it is overestimated by the classic ATC model. The effect of phenology changes on LST is smaller in the nighttime than in the daytime; therefore, the PATC model improves less RMSE compared with classic ATC at night. The improved RMSEs of grassland, cropland, and forest are 0.7, 0.6, and 0.3 K, respectively (see in Fig. 5). In addition to the LST variations caused by the phenology change, PATC can also catch the short-term LSTs fluctuation caused by local weather change. As shown in Fig. 5(a1), PATC model better simulates the temperature fluctuations caused by local weather changes, and the temperature fluctuations at night are smaller but can also be captured by PATC [see in Fig. 5(b)].

B. Accuracy Improvement Compared With ATCE

PATC and ATCE models take the same data as input, and both take the effects of phenology change and weather condition on LSTs into account. The main difference between two models is that PATC is based on an LTMM [35], [51], which separates the effects of phenology change and weather conditions, while ATCE combines the effects of phenology change and weather conditions together [46]. Here, we compare PATC with ATCE via the evaluation indicator of Drmse (referenced to ATCE) to explore whether the LTMM-based PATC model is superior to ATCE, wherein a higher Drmse value indicates better performance of PATC compared with ATCE. In this section, we calculate different Drmses among different NDVI ranges. Specifically, time series observations are classified by different NDVI ranges to calculate Drmses.

Different Drmses corresponding to different NDVI ranges indicate that PATC performs better than ATCE, with a mean Drmse value of 0.3 and 0.1 K in the daytime and nighttime, respectively. As shown in Fig. 6(a), in all land cover types, the predicted LSTs of which the corresponding NDVI values ranging from 0.8 to 1.0 have higher Drmses than other predictions in the daytime; the mean Drmses of urban, cropland, grassland, forest, and savanna are 2.4, 2.2, 1.3, 0.7, and 0.8 K, respectively. When the NDVI values range from 0.6 to 0.8, the Drmses of urban, cropland, and grassland are still higher than predictions of which the corresponding NDVI values are less than 0.6. When the NDVI value ranges from 0 to 0.2, the Drmses of cropland and grassland are lower than those of which the NDVI is larger than 0.6 but are still slightly higher than those of which the NDVI value is ranging from 0.2 to 0.6. Therefore, we can summarize that a higher NDVI value indicates a higher improvement of PATC compared with ATCE in the daytime; however, when the NDVI value is less than 0.2, PATC still performs better than ATCE with a mean Drmse of 0.5 K.

The superiority of PATC compared with ATCE in the nighttime is not as obvious as that in the daytime. As shown in Fig. 6(b), the mean Drmse of all land cover types is only 0.1 K, and the Drmses of all land cover types almost keep the same in different NDVI ranges. However, when the NDVI values are less than 0.2, forest and savanna have a higher Drmse than other land cover types, which might be because the proportions of these two types are quite low. Moreover, the lower improvement of PATC compared with ATCE in the nighttime is because both PATC and ATCE consider the effect of local weather; so they can simulate the local fluctuations caused by weather conditions in nighttime. However, the difference of LST between nocturnal vegetation and bare soil is small; so the mixed pixel LST is less affected by vegetation phenology changes.

To explore the spatial distribution of Drmses in different NDVI ranges in the daytime, we also supply the spatial patterns of Drmse. As shown in Fig. 7(f), the mean Drmse of all predictions is 0.3 K, and the higher Drmse occurs in the northwest and southwest of the study area of which the land cover types are mainly grassland and cropland. As shown in Fig. 7(a), when the NDVI value is less than 0.2, there are some pixels that lack observations and these pixels are mainly cropland and forest. The mean Drmse is 0.5 K which indicates a satisfying improvement of PATC compared with ATCE; moreover, the higher Drmses located in the northwest of this study area are mainly grassland, and the maximum even reaches to 6.1 K [see Fig. 7(a)]. When the NDVI values range from 0.2 to 0.4, the improvement of

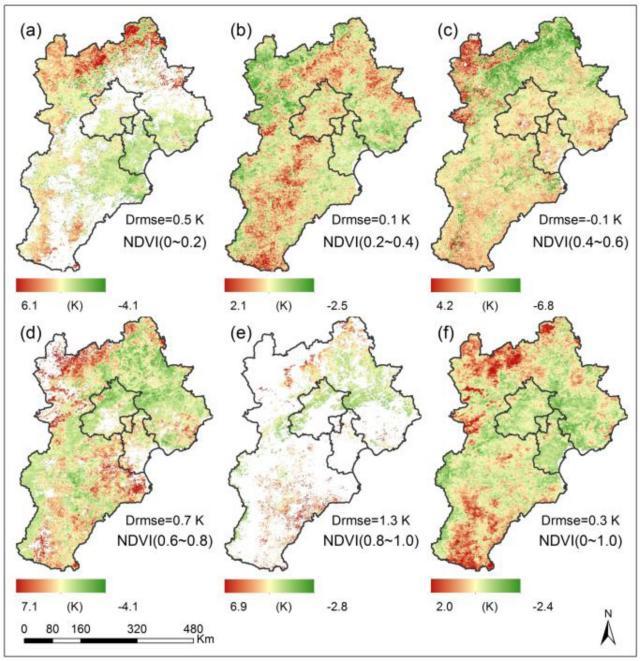

Fig. 7. Drmse (referenced to ATCE) of PATC in the daytime. (a)−(e) Drmses corresponding to different NDVI ranges.

PATC is unobvious, the mean Drmse is only 0.1 K, and higher Drmses mainly occur in cropland, and the maximum Drmse is only 2.1 K [see in Fig. 7(b)]. When the NDVI values range from 0.4 to 0.6, even PATC performs poorer than ATCE, and the mean Drmse is −0.1 K [see in Fig. 7(c)]. However, when the NDVI value is larger than 0.6, the superiority of PATC compared with ATCE is obvious. As shown in Fig. 7(d) and (e), when the NDVI values range from 0.6 to 0.8, the mean Drmse is 0.7 K, and the maximum Drmse reaches 7.1 K; when the NDVI values range from 0.8 to 1.0, the mean Drmse is 1.3 K, and the higher Drmses mainly occur in cropland and grassland. In summary, PATC performs better than ATCE in most situations, especially when the NDVI is larger than 0.6 but slightly poorer when the NDVI value ranges from 0.4 to 0.8.

In addition to comparing Drmses among different NDVI ranges, we also want to explore the relationship between Drmse and annual change rate of NDVI. Here, we use the annual mean derivate of NDVI (NDVI') to represent the annual change rate of NDVI, of which a larger value indicates a more complex annual change of NDVI. As shown in Fig. 8, Drmse is positively correlated with the annual mean derivate of NDVI in both daytime and nighttime. However, the slope of their relationship is larger in the daytime and smaller in the nighttime, with value of 0.99 for the daytime and 0.03 for the nighttime. The results indicate that the phenology change has a larger influence on PATC in the daytime than in nighttime. Moreover, the more complex the phenology change, the superior the performance of PATC compared with that of ATCE.

To compare PATC and ATCE temporally, we selected eight pixels with different phenology changes to show their daily absolute error (AE). As shown in Fig. 9(a), when the cropland enters its start of season in the early summer, the difference between the AEs of ATCE and PATC begins to increase; when the cropland enters its EOS in autumn, the difference between the AEs of ATCE and PATC begins to decrease, which indicates a better performance of PATC in densely vegetation covered seasons. Moreover, when the growing season lasts longer, the superiority of PATC lasts longer [see Fig. 9(b)]. When there are two growing seasons in one year, the difference of the performances of PATC among different NDVI values is similar to those in Fig. 9(a) and (b), i.e., the superiority of PATC is obvious in densely vegetation covered seasons and unobvious in sparsely vegetation covered seasons [see Fig. 9(c) and (d)]. In the urban area, the annual change rate of NDVI is small. Even though PATC sometimes performs better than ATCE in summer, it also performs poorer than ATCE sometimes, which indicates a less robustness of PATC over urban area [see Fig. 9(e) and (f)]. These pixels are all obtained from plain of which the elevations are all lower than 100 m. Hence, we also selected two pixels of grassland that is located in complex terrain, the elevations of which are higher than 100 m. As shown in Fig. 9(g) and (h), the superiority of PATC lasts during the growing season of vegetation. In addition, PATC also performs better than ATCE in winter of which the NDVI is low, which indicates the better performance of PATC is because PATC can well simulate the temperature fluctuations caused by local weather change.

In summary, above results indicate a superior performance of PATC compared with ATCE, especially during the growing season of vegetation in the daytime. Moreover, PATC can also well simulate the temperature fluctuations caused by local weather change when the vegetation is sparsely covered.

V. Discussion

This section aims to discuss the performance of PATC under different observations and the influence of filtered NDVI on the model performance. In this section, six pixels are randomly selected from different land cover types, of which two pixels are cropland, and the other four pixels are forest, grassland, savanna, and urban. For each pixel, we randomly selected 12, 16, 20, 40, 80, and 160 observations and then used the least squares fitting to compute model parameters of the temperature cycle model with the selected observations. To prevent that almost all observations are in the same month which leads to the ATC models not being able to catch the variation of LSTs at annual scale, we made sure that every season has randomly selected observations, especially when the observations are less than 20. According to the simulation results, the fitting accuracy of the temperature cycle model is gradually improved with the increase of observations. As shown in Fig. 10, the RMSE of PATC is smaller than that of ATCE and ATC under different observations wherein the ATC model has the lowest accuracy. In addition, the accuracies of ATC and ATCE change slightly with the observation counts. The difference between the highest and lowest accuracies of ATC is 0.3 K, that of ATCE is 0.4 K, while that of PATC is 1.0 K. When the observation count is 12, the accuracy of PATC is close to that of ATCE, with a difference of 0.05 K. However, when the observation count increases to 16, the

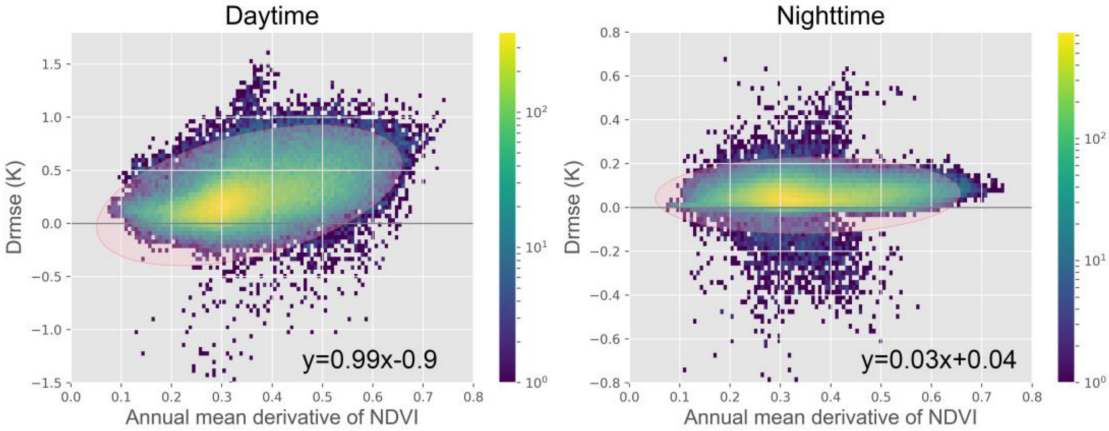

Fig. 8. Scatter plot between Drmse (referenced to ATCE) and the annual mean derivative of NDVI in the daytime and nighttime, respectively.

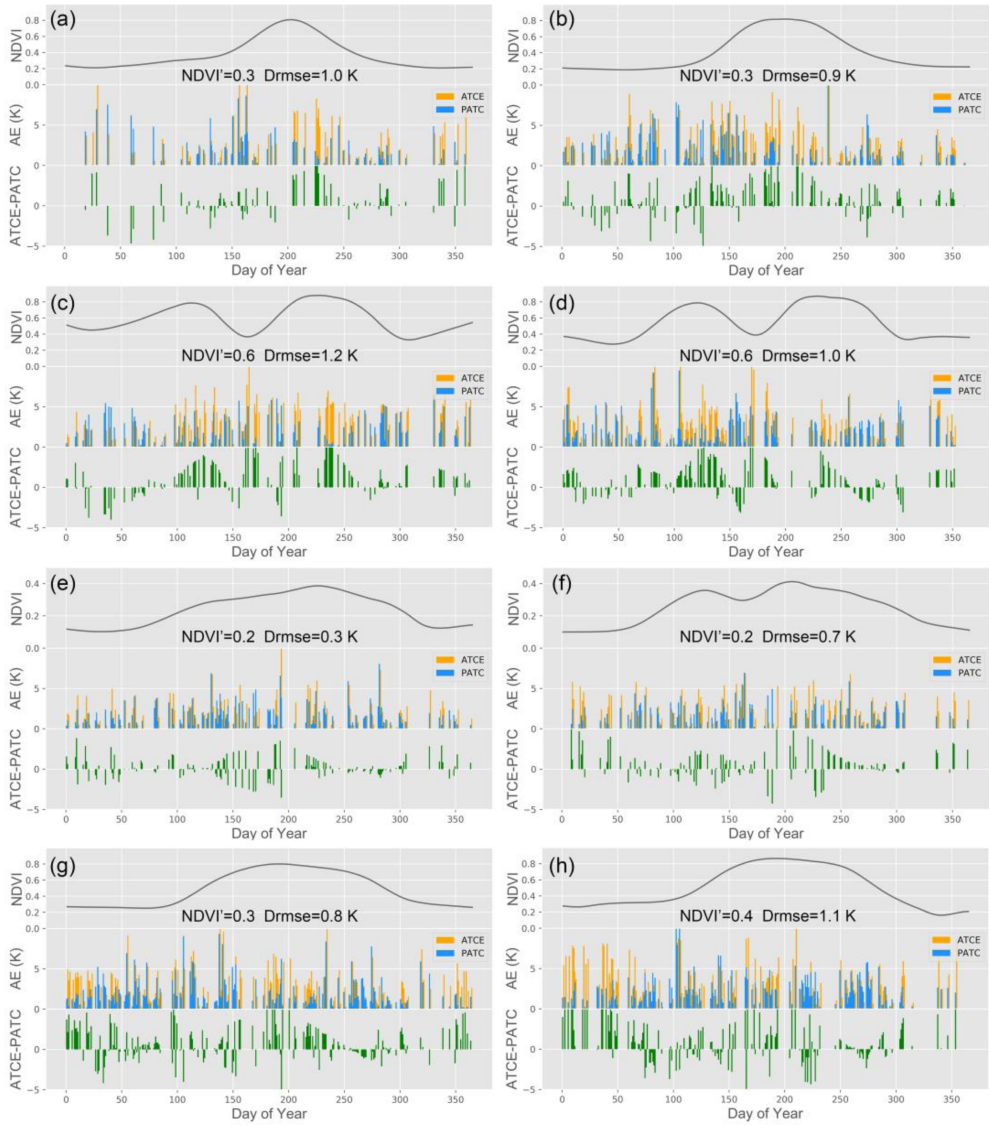

Fig. 9. Comparisons of model performances of PATC and ATCE in daytime. (a)−(d) Cropland. (e)−(f) Urban. (g)−(h) Grassland.

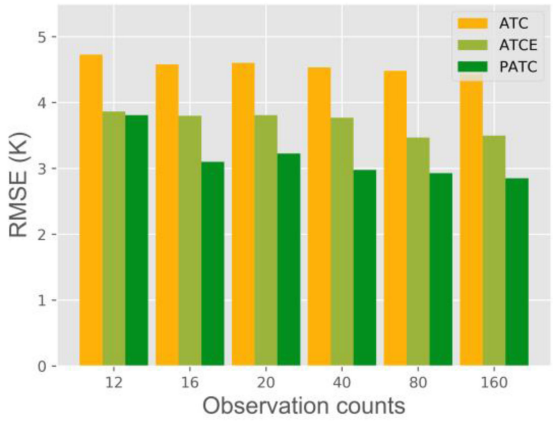

Fig. 10. RMSE of different ATC models with different observations.

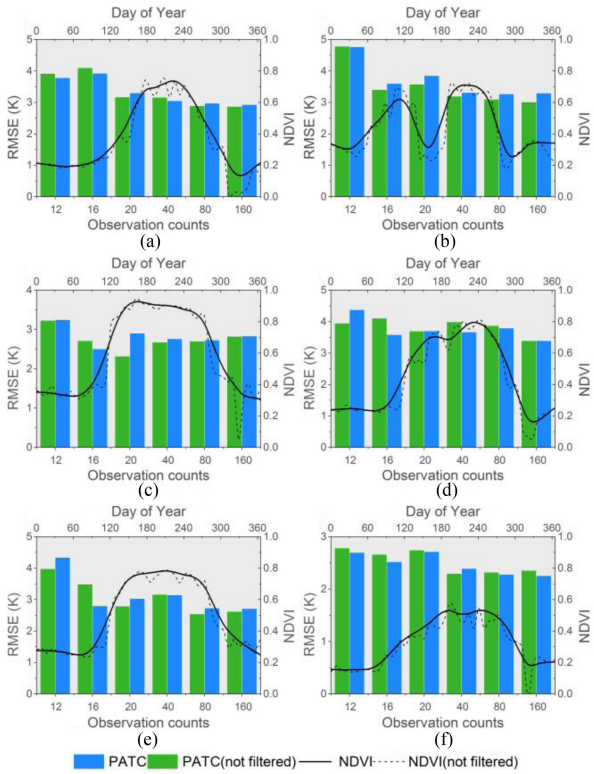

Fig. 11. RMSEs of PATC with different observations. (a) Cropland 1. (b) Cropland 2. (c) Forest. (d) Grassland. (e) Savanna. (f) Urban.

accuracy of PATC is significantly higher than that of ATCE, with a difference of 0.7 K. However, with the subsequent increase of the observations, the accuracy of PATC only fluctuates slightly. Even though more observations can bring better performance of PATC, 16 observations are sufficient to present the performance of PATC.

In addition, we also discuss the influence of filtered NDVI on the model performance. In this section, in addition to using the filtered NDVI sequence to test the performance of temperature cycle model, we also use unfiltered NDVI as control group. As shown in Fig. 11, the influences of filtered NDVI and not filtered NDVI on PATC vary with different observation counts. As shown in Fig. 11(a), when the observation count is small,

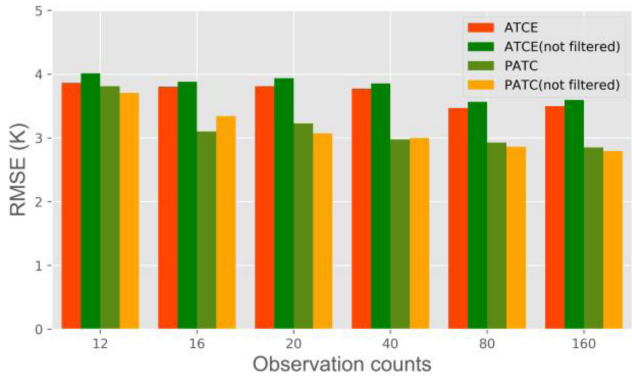

Fig. 12. RMSEs of ATCE and PATC with different observations.

the filtered NDVI can slightly improve PATC's accuracy, but when the observation count increases, the filtered NDVI has a poorer accuracy than the unfiltered NDVI. In addition, when the NDVI change is complex in a year, the filtered NDVI losing too much information will lead to a poorer performance of PATC compared with the unfiltered NDVI [see Fig. 11(b)]. Although whether the NDVI is filtered or not has a small influence on PATC totally, when the observations reach 16, the filtered NDVI can increase the accuracy by 0.14 K on average compared with the unfiltered NDVI.

Compared with PATC, the filtered NDVI has a greater influence on ATCE model. As shown in Fig. 12, the filtered NDVI can improve the accuracy of ATCE by 0.1 K on average compared with the unfiltered NDVI, while for the PATC, the filtered NDVI even reduces the accuracy of PATC by 0.02 K compared with the unfiltered NDVI. This is because the ATCE puts the influence of NDVI on temperature into the local fluctuation of temperature; so the local fluctuation of NDVI has a greater influence on the ATCE. On the contrary, the PATC puts the influence of NDVI on temperature into the annual oscillation of the temperature cycle model; so the local NDVI fluctuation has less influence on the PATC.

In conclusion, the above model tests suggest that PATC is robust to the filtered or not filtered NDVI sequences. Moreover, a limited observation with a count that reaches 16 can well present the performance of PATC, which indicates a promising application of PATC in LSTs of polar satellites, such as Landsat.

VI. Conclusion

In this article, we propose a PATC that takes the impacts of vegetation phenology and local weather changes into account. This model is based on a linear hybrid model of temperature. It is assumed that the temperature of the mixed pixel is composed of linear mixture of vegetation fractions and nonvegetation fractions, as well as short-term fluctuations caused by local weather conditions.

Here, we use MODIS LSTs to evaluate the performance of PATC and compare it with the classical ATC model and ATCE model. Compared with the classic ATC model, PATC can improve the accuracy by 1.6 and 0.5 K in the daytime and

nighttime, respectively. Compared with ATCE model, PATC can improve the mean accuracy by 0.3 and 0.1 K in daytime and nighttime, respectively. Specifically, the superiority of PATC compared with ATCE is especially obvious during the densely vegetation covered seasons in the daytime, the Drmse of which the corresponding NDVI ranging from 0.8 to 1.0 is 1.3 K. Comparisons with ATC and ATCE suggest the superiority of PATC in modeling daily LSTs.

In addition, with the selected samples, we find the performance of PATC is robust when the number of observations reaches 16, and the filtered NDVI can also slightly improve the performance of PATC when the observation count is 16. Future research may incorporate Landsat observations and DTC models to implement temporal interpolation of LSTs at diurnal scale.

ACKNOWLEDGMENT

The authors would like to thank the anonymous reviewers for helping to improve this manuscript.

REFERENCES

[1] M. C. Anderson, R. G. Allen, A. Morse, and W. P. Kustas, "Use of Landsat thermal imagery in monitoring evapotranspiration and managing water resources," *Remote Sens. Environ.*, vol. 122, pp. 50–65, 2012.

[2] S. Stisen, I. Sandholt, A. Nørgaard, R. Fensholt, and K. H. Jensen, "Combining the triangle method with thermal inertia to estimate regional evapotranspiration—Applied to MSG-SEVIRI data in the senegal river basin," *Remote Sens. Environ.*, vol. 112, no. 3, pp. 1242–1255, 2008.

[3] C. Cammalleri *et al.*, "Applications of a remote sensing-based two-source energy balance algorithm for mapping surface fluxes without in situ air temperature observations," *Remote Sens. Environ.*, vol. 124, pp. 502–515, 2012.

[4] J. Quan, Y. Chen, W. Zhan, J. Wang, J. Voogt, and M. Wang, "Multi-temporal trajectory of the urban heat island centroid in Beijing, China based on a Gaussian volume model," *Remote Sens. Environ.*, vol. 149, pp. 33–46, 2014.

[5] Q. Meng, L. Zhang, Z. Sun, F. Meng, L. Wang, and Y. Sun, "Characterizing spatial and temporal trends of surface urban heat island effect in an urban main built-up area: A 12-year case study in Beijing, China," *Remote Sens. Environ.*, vol. 204, pp. 826–837, 2017.

[6] H. Xia, Y. Chen, and J. Quan, "A simple method based on the thermal anomaly index to detect industrial heat sources," *Int. J. Appl. Earth Observ. Geoinform.*, vol. 73, pp. 627–637, 2018.

[7] L. Sun *et al.*, "Reconstructing daily clear-sky land surface temperature for cloudy regions from MODIS data," *Comput. Geosci.*, vol. 105, pp. 10–20, 2017.

[8] W. L. Crosson, M. Z. Al-Hamdan, S. N. J. Hemmings, and G. M. Wade, "A daily merged MODIS aqua–terra land surface temperature data set for the conterminous united states," *Remote Sens. Environ.*, vol. 119, pp. 315–324, 2012.

[9] S.-B. Duan, Z.-L. Li, and P. Leng, "A framework for the retrieval of all-weather land surface temperature at a high spatial resolution from polar-orbiting thermal infrared and passive microwave data," *Remote Sens. Environ.*, vol. 195, pp. 107–117, 2017.

[10] X. Zhang, J. Zhou, S. Liang, and D. Wang, "A practical reanalysis data and thermal infrared remote sensing data merging (RTM) method for reconstruction of a 1-km all-weather land surface temperature," *Remote Sens. Environ.*, vol. 260, pp. 112437,2021.

[11] C. Zhang, W. Li, and D. Travis, "Gaps-fill of SLC-off Landsat ETM+ satellite image using a geostatistical approach," *Int. J. Remote Sens.*, vol. 28, no. 22, pp. 5103–5122, 2007.

[12] F.-W. Chen and C.-W. Liu, "Estimation of the spatial rainfall distribution using inverse distance weighting (IDW) in the middle of Taiwan," *Paddy Water Environ.*, vol. 10, no. 3, pp. 209–222, 2012.

[13] Z. Liu, P. Wu, S. Duan, W. Zhan, X. Ma, and Y. Wu, "Spatiotemporal reconstruction of land surface temperature derived from fengyun geostationary satellite data," *IEEE J. Sel. Topics Appl. Earth Observ. Remote Sens.*, vol. 10, no. 10, pp. 4531–4543, Oct. 2017.

[14] L. Ke, X. Ding, and C. Song, "Reconstruction of time-series MODIS LST in central Qinghai-Tibet plateau using geostatistical approach," *IEEE Geosci. Remote Sens. Lett.*, vol. 10, no. 6, pp. 1602–1606, Nov. 2013.

[15] X.-M. Fan, H.-G. Liu, G.-H. Liu, and S.-B. Li, "Reconstruction of MODIS land-surface temperature in a flat terrain and fragmented landscape," *Int. J. Remote Sens.*, vol. 35, no. 23, pp. 7857–7877, 2014.

[16] J. Chen, X. Zhu, J. E. Vogelmann, F. Gao, and S. Jin, "A simple and effective method for filling gaps in Landsat ETM+ SLC-off images," *Remote Sens. Environ.*, vol. 115, no. 4, pp. 1053–1064, 2011.

[17] X. Zhu, D. Liu, and J. Chen, "A new geostatistical approach for filling gaps in Landsat ETM+ SLC-off images," *Remote Sens. Environ.*, vol. 124, pp. 49–60, 2012.

[18] C. Zeng, H. Shen, and L. Zhang, "Recovering missing pixels for Landsat ETM+ SLC-off imagery using multi-temporal regression analysis and a regularization method," *Remote Sens. Environ.*, vol. 131, pp. 182–194, 2013.

[19] T. Shuai *et al.*, "A spectral angle distance-weighting reconstruction method for filled pixels of the MODIS land surface temperature product," *IEEE Geosci. Remote Sens. Lett.*, vol. 11, no. 9, pp. 1514–1518, Sep. 2014.

[20] C. Zeng, D. Long, H. Shen, P. Wu, Y. Cui, and Y. Hong, "A two-step framework for reconstructing remotely sensed land surface temperatures contaminated by cloud," *ISPRS J. Photogrammetry Remote Sens.*, vol. 141, pp. 30–45, 2018.

[21] Z. Chao, S. Huanfeng, Z. Mingliang, Z. Liangpei, and W. Penghai, "Reconstructing MODIS LST based on multitemporal classification and robust regression," *IEEE Geosci. Remote Sens. Lett.*, vol. 12, no. 3, pp. 512–516, Mar. 2015.

[22] D. J. Weiss, P. M. Atkinson, S. Bhatt, B. Mappin, S. I. Hay, and P. W. Gething, "An effective approach for gap-filling continental scale remotely sensed time-series," *ISPRS J. Photogrammetry Remote Sens.*, vol. 98, pp. 106–118, Dec 2014.

[23] Z. Liu *et al.*, "Balancing prediction accuracy and generalization ability: A hybrid framework for modelling the annual dynamics of satellite-derived land surface temperatures," *ISPRS J. Photogrammetry Remote Sens.*, vol. 151, pp. 189–206, 2019.

[24] X. Li, Y. Zhou, G. R. Asrar, and Z. Zhu, "Creating a seamless 1 km resolution daily land surface temperature dataset for urban and surrounding areas in the conterminous united states," *Remote Sens. Environ.*, vol. 206, pp. 84–97, 2018.

[25] P. Fu and Q. Weng, "Temporal dynamics of land surface temperature from Landsat TIR time series images," *IEEE Geosci. Remote Sens. Lett.*, vol. 12, no. 10, pp. 2175–2179, Oct. 2015.

[26] H. Ghafarian Malamiri, I. Rousta, H. Olafsson, H. Zare, and H. Zhang, "Gap-filling of MODIS time series land surface temperature (LST) products using singular spectrum analysis (SSA)," *Atmosphere*, vol. 9, no. 9, pp. 334, 2018.

[27] P. Gething *et al.*, "Global data for ecology and epidemiology: A novel algorithm for temporal Fourier processing MODIS data," *PloS One*, vol. 3, no. 1, pp. e1408, 2008.

[28] F. Aires, C. Prigent, and W. B. Rossow, "Temporal interpolation of global surface skin temperature diurnal cycle over land under clear and cloudy conditions," *J. Geophys. Res.: Atmos.*, vol. 109, no. D4, 2004.

[29] B. Bechtel, "Robustness of annual cycle parameters to characterize the urban thermal landscapes," *IEEE Geosci. Remote Sens. Lett.*, vol. 9, no. 5, pp. 876–880, Sep. 2012.

[30] Y. Xu and Y. Shen, "Reconstruction of the land surface temperature time series using harmonic analysis," *Comput. Geosci.*, vol. 61, pp. 126–132, 2013.

[31] Q. Weng and P. Fu, "Modeling annual parameters of clear-sky land surface temperature variations and evaluating the impact of cloud cover using time series of Landsat TIR data," *Remote Sens. Environ.*, vol. 140, pp. 267–278, 2014.

[32] D. Sun and R. T. Pinker, "Implementation of GOES-based land surface temperature diurnal cycle to AVHRR," *Int. J. Remote Sens.*, vol. 26, no. 18, pp. 3975–3984, 2005.

[33] F.-M. Göttsche and F.-S. Olesen, "Modelling the effect of optical thickness on diurnal cycles of land surface temperature," *Remote Sens. Environ.,* vol. 113, no. 11, pp. 2306–2316, 2009.

[34] J. Zhou, Y. Chen, X. Zhang, and W. Zhan, "Modelling the diurnal variations of urban heat islands with multi-source satellite data," *Int. J. Remote Sens.*, vol. 34, no. 21, pp. 7568–7588, 2013.

[35] J. Quan, Y. Chen, W. Zhan, J. Wang, J. Voogt, and J. Li, "A hybrid method combining neighborhood information from satellite data with modeled diurnal temperature cycles over consecutive days," *Remote Sens. Environ.*, vol. 155, pp. 257–274, 2014.

[36] F. Hong *et al.*, "Comprehensive assessment of four-parameter diurnal land surface temperature cycle models under clear-sky," *ISPRS J. Photogrammetry Remote Sens.*, vol. 142, pp. 190–204, 2018.
[37] W. Zhan *et al.*, "Interpolating diurnal surface temperatures of an urban facet using sporadic thermal observations," *Building Environ.*, vol. 57, pp. 239–252, 2012.
[38] F. Huang, W. Zhan, S.-B. Duan, W. Ju, and J. Quan, "A generic framework for modeling diurnal land surface temperatures with remotely sensed thermal observations under clear sky," *Remote Sens. Environ.*, vol. 150, pp. 140–151, 2014.
[39] H. Xia, Y. Chen, Y. Li, and J. Quan, "Combining kernel-driven and fusion-based methods to generate daily high-spatial-resolution land surface temperatures," *Remote Sens. Environ.*, vol. 224, pp. 259–274, 2019.
[40] J. Quan, W. Zhan, T. Ma, Y. Du, Z. Guo, and B. Qin, "An integrated model for generating hourly Landsat-like land surface temperatures over heterogeneous landscapes," *Remote Sens. Environ.*, vol. 206, pp. 403–423, 2018.
[41] F. Huang *et al.*, "Temporal upscaling of surface urban heat island by incorporating an annual temperature cycle model: A tale of two cities," *Remote Sens. Environ.*, vol. 186, pp. 1–12, 2016.
[42] H. Liu and Q. Weng, "Enhancing temporal resolution of satellite imagery for public health studies: A case study of West Nile virus outbreak in Los Angeles in 2007," *Remote Sens. Environ.*, vol. 117, pp. 57–71, 2012.
[43] J. Quan, W. Zhan, Y. Chen, M. Wang, and J. Wang, "Time series decomposition of remotely sensed land surface temperature and investigation of trends and seasonal variations in surface urban heat islands," *J. Geophys. Res.: Atmos.*, vol. 121, no. 6, pp. 2638–2657, 2016.
[44] B. Bechtel and P. Sismanidis, "Time series analysis of moderate resolution land surface temperatures," in *Remote Sensing Time Series Image Processing*. Boca Raton, FL, USA: CRC Press, 2017, pp. 111–142.
[45] P. Fu and Q. Weng, "Consistent land surface temperature data generation from irregularly spaced Landsat imagery," *Remote Sens. Environ.*, vol. 184, pp. 175–187, 2016.
[46] Z. Zou *et al.*, "Enhanced modeling of annual temperature cycles with temporally discrete remotely sensed thermal observations," *Remote Sens.*, vol. 10, no. 4, pp. 650, 2018.
[47] Z. Wan, "New refinements and validation of the collection-6 MODIS land-surface temperature/emissivity product," *Remote Sens. Environ.*, vol. 140, pp. 36–45, 2014.
[48] S.-B. Duan *et al.*, "Validation of collection 6 MODIS land surface temperature product using in situ measurements," *Remote Sens. Environ.*, vol. 225, pp. 16–29, 2019.
[49] H. Li *et al.*, "Temperature-Based and radiance-based validation of the collection 6 MYD11 and MYD21 land surface temperature products over barren surfaces in north western China," *IEEE Trans. Geosci. Remote Sens.*, vol. 59, no. 2, pp. 1794–1807, Feb. 2021.
[50] W. H. Press, B. P. Flannery, S. A. Teukolsky, and W. T. Vetterling, *Numerical Recipes in C: The Art of Scientific Computing*. Cambridge, NY, USA, USA: Cambridge Univ. Press, 1990.
[51] C. Deng and C. Wu, "Examining the impacts of urban biophysical compositions on surface urban heat island: A spectral unmixing and thermal mixing approach," *Remote Sens. Environ.*, vol. 131, pp. 262–274, 2013.
[52] W. Zhu, Y. Pan, H. He, L. Wang, M. Mou, and J. Liu, "A changing-weight filter method for reconstructing a high-quality NDVI time series to preserve the integrity of vegetation phenology," *IEEE Trans. Geosci. Remote Sens.*, vol. 50, no. 4, pp. 1085–1094, Apr. 2012.
[53] S. Peng *et al.*, "Surface urban heat island across 419 global big cities," *Environ. Sci. Technol.*, vol. 46, no. 2, pp. 696–703, Jan. 2012.
[54] J. Nichol, "Remote sensing of urban heat islands by day and night," *Photogrammetric Eng. Remote Sens.*, vol. 71, no. 5, pp. 613–622, 2005.
[55] A. Chudnovsky, E. Ben-Dor, and H. Saaroni, "Diurnal thermal behavior of selected urban objects using remote sensing measurements," *Energy Buildings*, vol. 36, no. 11, pp. 1063–1074, 2004.

Haiping Xia received the B.S. degree in geographic information system from School of Environment Science and Spatial Informatics, China University of Mining and Technology, Xuzhou, China, in 2015. She is currently working toward the Ph.D. degree in methodology and its application of spatiotemporal downscaling of land surface temperature at the State Key Laboratory of Remote Sensing Science, Faculty of Geographical Science, Beijing Normal University, Beijing, China.

Her research interests include thermal sharpening and analysis on urban thermal environment.

Yunhao Chen received the B.S. and M.S. degrees in resource management from the Anhui University of Science and Technology, Huainan, China, in 1994 and 1997, respectively, and the Ph.D. degree in geodetic engineering from the China University of Mining and Technology, Beijing, China, in 1999.

From 2000 to 2001, he did postdoctoral research with Beijing Normal University, Beijing, China. Since 2001, he has been with the Faculty of Geographical Science, Beijing Normal University, where he is currently a Professor with the State Key Laboratory of Remote Sensing Science. His research interests include thermal remote sensing of urban environment and applications of remote sensing in ecology.

Adu Gong received the B.S. degree in land use and land planning from Southwest University, Chongqing, China, in 1998, the M.S. degree in soil and water conservation from Chinese Academy of Sciences/Ministry of Water Resources Chengdu Institute of Mountain Hazards and Environment, Chengdu, China, in 2001, and the Ph.D. degree in geography from Beijing Normal University, Beijing, China, in 2005.

He is currently an Associate Professor with the Faculty of Geographical Science and State Key Laboratory of Remote Sensing Science, Beijing Normal University. His research interests include thermal remote sensing and urban heat island.

Kangning Li received the B.S. degree in geographic information system from the College of Urban and Environmental Science, Northwest University, Xi'an, China, in 2016. She is currently working toward the Ph.D. degree in studies on urban heat island at a global scale at the State Key Laboratory of Remote Sensing Science, Faculty of Geographical Science, Beijing Normal University, Beijing, China.

Her research interests include thermal remote sensing of urban environment.

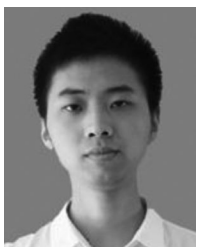

Long Liang received the B.S. degree in remote sensing science and technology from the School of Geosciences and Surveying Engineering, China University of Mining and Technology, Beijing, China, in 2018. He is currently working toward the Ph.D. degree at the State Key Laboratory of Remote Sensing Science, Faculty of Geographical Science, Beijing Normal University, Beijing, China.

His research interests include thermal sharpening and risk assessment of natural disaster on heritages.

Zheng Guo received the B.S. degree in horticultural from China Agricultural University, Beijing, China, in 2007, the M.S. degree in ecology from Zhejiang A&F University, Zhejiang, China, in 2010, and the Ph.D. degree in geography from Beijing Normal University, Beijing, in 2013.

He is a Senior Engineer with the Division of Remote Sensing Data Application, National Satellite Meteorological Center, China Meteorological Administration, Beijing, China. His research interests include thermal remote sensing and applications for thermal environment of the city and atmospheric pollutants monitored by remote sensing.